3.22 NMR-Spektroskopie Fortgeschrittenenpraktikum: Abteilung B Fachbereich Physik

TECHNISCHE
UNIVERSITÄT
DARMSTADT

Diese Versuchsanleitung basiert auf der Grundlage aus 2015 von Dr. Oleg Petrov und ist deshalb auf Englisch. Die Sprache für das Protokoll sowie für die Durchführung kann zwischen Deutsch oder Englisch gewählt werden. Zur Vorbereitung dient das angehängt Skript "NMR-Spektroskopie: An Introduction" sowie die darin enthaltenen Quellen, auch Teile der Versuchsanleitung 3.10 können herangezogen werden. Das Skript beinhaltet alle notwendigen Grundlagen für diesen Versuch, wobei die Kapitel 2.2 (Electric quadrupole coupling), 2.4 (J-coupling) und 2.5 (Anisotropy of spin interactions) über den Versuch hinausgehen. Ein tieferes Verständnis dieser Themen ist daher nicht erforderlich.

^{19}F NMR spectroscopy for the study of anion dynamics in the superionic conductor LaF$_3$

LaF$_3$ as a superionic conductor

Lanthanum trifluoride, LaF$_3$ has attained some interest because of its unusually high fluorine ionic conductivity. Apart from applications of LaF$_3$ as sensors or even as solid electrolyte in fuel cells the system represents a very nice model system for studying elementary processes of the fluorine dynamics. LaF$_3$ exhibits the so called tysonite crystal structure (Fig. 1).
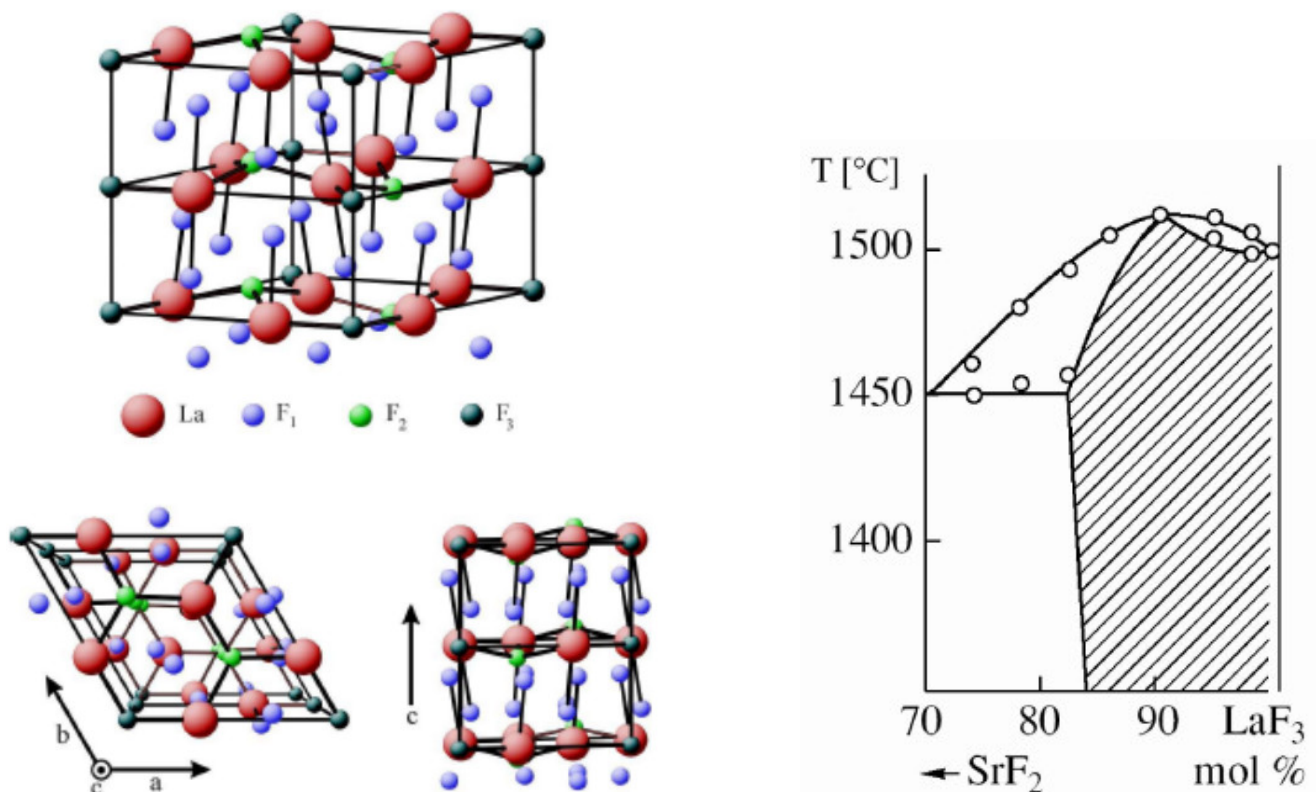

Abbildung 1: (a) LaF$_3$ crystal structure (from [1]). (b) Phase diagram of the system LaF$_3$-SrF$_2$. The shaded area indicates the regime of a homogeneous tysonite structure.
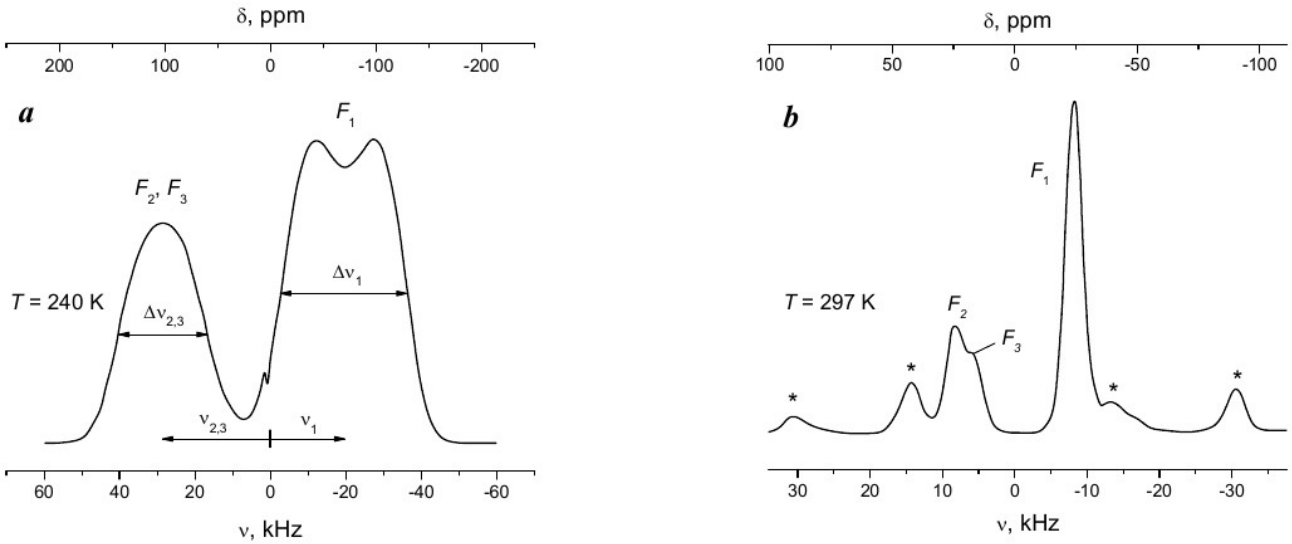
Abbildung 2: (a) ^{19}F NMR static spectrum of LaF$_3$ monocrystal acquired at an operating frequency for ^{19}F of 282 MHz (from [1]). (b) ^{19}F NMR magic-angle spinning spectrum of polycrystalline LaF$_3$ collected with a spinning speed of 23 kHz (* = spinning sidebands). A spectrometer frequency for ^{19}F was 338.75 MHz (from [2]).

There are three crystallographically distinct sites for fluorine, F_1, F_2 and F_3, with multiplicities of 6:2:1. The F_1 ions form a layered structure perpendicular to the c-axis, whereas the F_2 and F_3 ions create a tunnel structure along the c-axis. The sub-lattices F_1, F_2 and F_3 differ with respect to fluorine-ion mobility. Namely, one distinguishes between ion jumps within the F_1 sub-lattice and the exchange between the F_1 and $F_{2,3}$ sub-lattices, described by characteristic correlation times τ_{11} and τ_{12} and τ_{13}, respectively. The dynamics within the F_1 sub-lattice is always faster than the exchange dynamics, that is, $\tau_{11} < \tau_{12}$ and $\tau_{11} < \tau_{13}$.

Interesting phenomena appear in heterovalently doped LaF$_3$ crystals, such as La$_{1-x}$Sr$_x$F$_{3-x}$. The SrF$_2$-doped crystal keeps the same tysonite structure up to 16 mol% of SrF$_2$ (Fig. 1). Replacing a three-valent La ion by a two-valent Sr ion creates a vacancy among the fluorine positions. Vacancies on the F_1 sub-lattice were observed in a neutron diffraction study of a similar BaF$_2$-doped LaF$_3$ crystal [2]. Due to the existence of such vacancies the fluorine dynamics becomes much faster compared to a pure LaF$_3$ [3].

^{19}F NMR spectra of LaF$_3$ and LaF$_3$-SrF$_2$ crystals

Fluorine ions in the positions F_1 and $F_{2,3}$ are identified in ^{19}F NMR spectrum by their different chemical shifts. Figure 2 shows an ^{19}F NMR spectrum of a pure LaF$_3$ crystal at 240 K, with c-axis oriented along to the B_0 field. Two spectral components have an intensity ratio of 2:1, according to the number of fluorine-ions in F_1 and $F_{2,3}$ groups. Thus, the lower frequency resonance is assigned to the F_1 ions and that at higher frequency to the $F_{2,3}$ ions. The exact positions of the resonances, ν_1 and $\nu_{2,3}$, depend on the crystal orientation inside the NMR coil, due to the chemical shift anisotropy (see Section 2 in the Introduction). The resonance widths, $\Delta\nu_1$ and $\Delta\nu_{2,3}$, are controlled by the dipole-dipole interaction between fluorine nuclei. The splitting of the F_1 signal is caused by a dominant dipolar coupling of the nearest-neighbouring spin pairs along the c-axis (see Fig. 1). The chemical shift difference between F_2 and F_3 ions is less than 15 ppm, so they are not resolved in the wide-line spectrum in Fig. 2a. They can be resolved, however, in a magic-angle spinning (MAS) spectrum in which the dipole-dipole line broadening is vastly reduced (Fig. 2b).

The dipole-dipole splitting of the F_1 resonance visible in Fig. 2a says that the rate of ion jumping at 240 K does not exceed the spectrum of dipole-dipole interactions, that is, $\tau_{11}^{-1} \leq 2\pi\Delta\nu_1$. When the temperature rises, the ion jumps in the F_1 sub-lattice become faster. The dipole-dipole interactions between the ions fluctuate at higher frequency and eventually average out as the jump rate τ_{11}^{-1} approaches the limit $\tau_{11}^{-1} \gg 2\pi\Delta\nu_1$. In consequence, the F_1 resonance gets narrowed ("motional narrowing"), as seen in Fig. 3. In this system (pure LaF$_3$), the averaging commences at ≈ 330 K, and a minimum line width is observed at ≈ 525 K. On the other hand, the $F_{2,3}$ resonance does not exhibit the motional narrowing in the given temperature range. One may conclude, therefore, that the movement of F_2 and F_3 ions along their tunnel structures remains slow ("frozen") on the NMR time scale, that is, $\tau_{22}^{-1}, \tau_{33}^{-1} < 2\pi\Delta\nu_{2,3}$. Above 525 K, the F_1 line starts broadening again (Fig. 3a) and shifts gradually towards the $F_{2,3}$ resonance. At ≈ 725 K, the two resonances coalesce into a single line with its further narrowing. This behaviour is a manifestation of the chemical exchange of ions
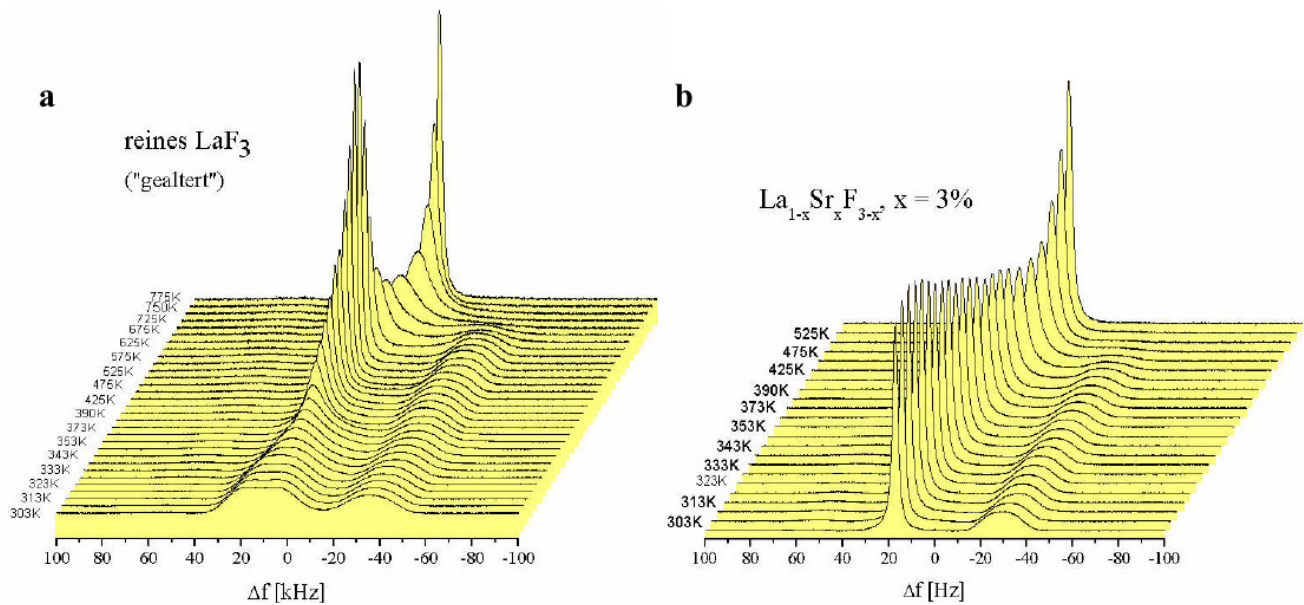
Abbildung 3: Variable temperature spectra of pure and 3 % doped LaF$_3$.

between the F_1 and $F_{2,3}$ sites (see Section 3.2 in the Introduction). The coalescence of the two resonances and the further narrowing occur when the exchange frequencies τ_{12}^{-1} and τ_{13}^{-1} become greater than the difference in the chemical shift.

It is expedient to denote the lower frequency resonance as F_A and the higher frequency resonance as F_B, to emphasise that at high temperatures, they no longer represent separate F_1 and $F_{2,3}$ positions but are average lines due to the chemical exchange of ions between those crystallographic sites.

The fluorine dynamics in Sr-doped LaF$_3$ (Fig. 3b) is faster than in pure LaF$_3$ (Fig. 3a), such that the resonance line of the F_1 ions narrows already at room temperature. The changes seen in Sr-doped LaF$_3$ spectra at elevated temperatures are solely due to the ion exchange between the F_1 and $F_{2,3}$ sub-lattices. A closer look at the spectra in Fig. 3b reveals a slightly different effect of the exchange on the F_A and F_B lines. While both lines shift towards one another upon warming, the F_A line becomes more intensive and the F_B line less intensive. The F_A line varies in width and the F_B line remains of virtually the same width. Such a behaviour can be explained assuming a different mobility for the $F_{2,3}$ ions, e.g. due to their different proximity to vacant sites in a doped crystal. Hence, at every particular temperature, only a fraction of the $F_{2,3}$ ions, $\Delta_{2,3} = \Delta_{2,3}(T)$, will be involved in the fast exchange with the F_1 ions. The position and the intensity of the average resonance (F_A) will change the more, the more $F_{2,3}$ ions get thermally-activated, that is, the greater $\Delta_{2,3}(T)$.

Experiment

The task consists of performing variable temperature ^{19}F NMR experiments on a doped LaF$_3$ crystal. Details (the choice of the sample, the temperature range to be covered, the temperature steps etc.) will be discussed with the supervisor of the lab course. The following tasks have to be performed:

- inserting the correctly oriented sample (c-axis parallel to the magnetic field direction) into the probe head

- tuning and matching the probe head

- optimisation of single-pulse sequence parameters (90°-pulse length, pulse repetition delay, NMR coil ring-down delay, etc.)

- measuring the FID signal at a room temperature T_{lab}

- setting the next temperature and allowing the sample to thermalize

- during the waiting time: processing spectra (FFT, phasing, baseline correction)

- repetition of this procedure for several temperatures

All results should be presented graphically. The experiment results in a set of variable-temperature spectra similar to Fig. 3b. The data evaluation includes measuring as a function of temperature:

- spectral line positions ν_A and ν_B,

- spectral line widths $\Delta\nu_A$ and $\Delta\nu_B$,

- spectral line integral intensities I_A and I_B normalized to the intensity of the whole spectrum.

Given these measurements and assuming the difference in mobility amid the $F_{2,3}$ ions, calculate:

- the fraction $\Delta_{2,3}$ of thermally-activated $F_{2,3}$ ions that contribute to the average resonance F_A,

- the position of the average resonance, ν_A^{calc},

- the Arrhenius activation energy E_A for the $F_{2,3}$ ions via a fit assuming the Arrhenius type dependence $\Delta_{2,3}(T) \propto \exp\left(-\frac{E_A}{k_B T}\right)$. Display the data and fit in an Arrhenius plot.

Neglect the temperature dependence of the chemical shift itself and use the following equations:

$$\Delta_{2,3}(T) = 1 - \frac{3\, I_B(T)}{I_B(T) + I_A(T)} \tag{1}$$

$$\nu_A^{calc}(T) = \frac{2\, \nu_1 + \Delta_{2,3}(T)\, \nu_{2,3}}{2 + \Delta_{2,3}(T)} \tag{2}$$

with the approximation $\nu_1 \approx \nu_A(T_{lab})$ und $\nu_{2,3} \approx \nu_B(T_{lab})$. Compare ν_A^{calc} with the measured positions ν_A of the average resonance. Draw a conclusion about the proposed model.

Literatur

[1] O. Lips. NMR-Untersuchungen an schnellen Ionenleitern vom LaF3-Typ. *Dissertation, TU Darmstadt*, 2004.

[2] F. Wang and C.P. Grey. Probing the mechanism of fluoride-ion conduction in LaF3 and strontium-doped LaF3 with high-resolution 19F MAS NMR. *Chem. Mater.*, 9(5):1068, 1997.

[3] F. Fujara, D. Kruk, O. Lips, A.F. Privalov, V. Sinitsyn, and H. Stork. Fluorine dynamics in LaF3-type fast ionic conductors – Combined results of NMR and conductivity techniques. *Solid State Ionics*, 179(40):2350, 2008.

Institut für Festkörperphysik - TU Darmstadt

Physikalisches Praktikum für Fortgeschrittene

3.22. NMR-Spektroskopie

(in Englisch)

An Introduction, compiled by Oleg V. Petrov

Version 2.0, March 2015

Contents

1. Nuclear Magnetic Resonance Phenomenon

1.1. Nuclear spins in a static magnetic field

Spin-bearing nuclei, e.g. ^{1}H, ^{7}Li, ^{13}C, ^{14}N, ^{19}F, ^{23}Na, ^{29}Si, ^{31}P, ^{35}Cl, ^{129}Xe, possess a magnetic dipole moment, $\boldsymbol{\mu}$,

$$\boldsymbol{\mu} = \gamma \mathbf{I} \tag{1}$$

related to their angular moment, or simply spin $\mathbf{I}$, via the gyromagnetic ratio γ. In an external magnetic field $\mathbf{B}_0$, the spins take on a most energy-favorable orientation which is either parallel or anti-parallel to $\mathbf{B}_0$ depending on the sign of γ. The alignment of spins in the $\mathbf{B}_0$ field gives rise to a net nuclear magnetization $\mathbf{M}$ (Fig. 1). This spin alignment, or spin polarization, in the external magnetic field is disturbed by thermal fluctuations. The net magnetization is therefore a trade-off between the $\mathbf{B}_0$ field strength and the thermal energy. This is expressed by Curie's law:

$$\mathbf{M} = C \frac{\mathbf{B}_0}{T} \tag{2}$$

where C is a material-specific Curie constant which depends on spin concentration and γ ($\propto \gamma^2$).

In thermal equilibrium, $\mathbf{M}$ is parallel to $\mathbf{B}_0$ (Fig. 1). If $\mathbf{M}$ makes an angle with $\mathbf{B}_0$, it will precess around $\mathbf{B}_0$ (alike a tilted gyroscope precessing in the gravitational field) with the angular frequency

$$\boldsymbol{\omega}_0 = -\gamma \mathbf{B}_0 \tag{3}$$

called the Larmor frequency (Fig. 2). Table A1 shows the Larmor frequencies for selected NMR-active nuclei at $B_0 = 8.75$ T. Given time, $\mathbf{M}$ attains its equilibrium state as the precessing spins exchange their energy with surrounding particles (the lattice). This process is called the spin-lattice relaxation.
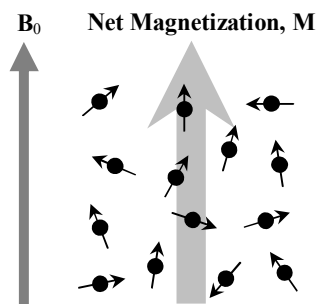

Fig.1. Polarization of nuclear spins in the external magnetic field $\boldsymbol{B_0}$ disturbed by internal interactions.
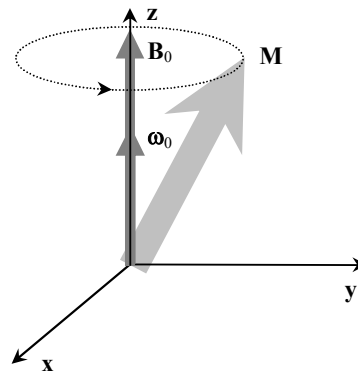
Fig.2. Precession of the net magnetization in the $\boldsymbol{B_0}$ field at a Larmor frequency $\boldsymbol{\omega_0} = -\gamma \boldsymbol{B_0}$ (the case of $\gamma < 0$).

1.2. Zeeman eigenstates and energy levels

The behavior of magnetic nuclei in applied fields is conveniently presented in energy level diagrams. The spin **I** is quantized according to the angular quantum number I (usually called spin too) such that a nucleus of spin I is found in one of $2I+1$ stationary states when placed in the magnetic field. The states are characterized by the magnetic quantum number m which takes on values $I, I–1, I–2, …, –I$, totally $2I+1$. They are called Zeeman eigenstates and symbolized as $|I,m\rangle$, or in the particular case of $I =$ 1/2, as $|\alpha\rangle$ and $|\beta\rangle$ for $m = +\frac{1}{2}$ and $-\frac{1}{2}$, respectively. The corresponding energies

$$E_m = -\gamma\hbar B_0 m \qquad (4)$$

are called Zeeman eigenvalues. From Eq. (4), the magnetic quantum number m defines the observable component of $\boldsymbol{\mu}$ along $\mathbf{B}_0 \parallel \mathbf{z}$, $\mu_z = \gamma\hbar m$.

Fig. 3 shows Zeeman energy diagrams for spins-1/2 and spins-1. The energy slit that separates Zeeman eigenstates with $\Delta m = 1$ is proportional to the $\mathbf{B}_0$ field strength according to Eq. (4):

$$\Delta E = \gamma\hbar B_0 \qquad (5)$$

NMR spectroscopy measures this difference in energy. From Eq. (3) and (5), the Larmor frequency relates to the energy slit ΔE as

$$\omega_0 = \Delta E / \hbar \qquad (6)$$

The macroscopic magnetization **M** is determined by the difference ΔN in spin populations of the Zeeman energy levels. In thermal equilibrium, ΔN is expressed via corresponding Boltzmann factors. For a two-level system of spins-1/2 we have:

$$\frac{N_\alpha}{N_\beta} = \frac{\exp(-E_\alpha / k_B T)}{\exp(-E_\beta / k_B T)} \quad \Rightarrow \quad \frac{\Delta N}{N_\alpha} = 1 - \exp(-\Delta E / k_B T) \qquad (7)$$

The energy split ΔE is small ($\sim 10^{-25}$ J) compared to the thermal energy, so is the difference in spin populations ($\sim 0.001\%$ at 300 K). Under condition $\Delta E << k_B T$, Eq. (7) reproduces the Curie's law, Eq. (2).
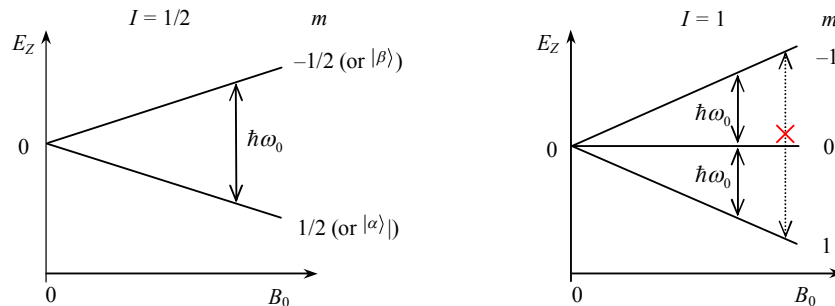

Fig. 3. Zeeman energy levels for spins-1/2 and spins-1 (the case of $\gamma > 0$). The solid arrows denote spin transitions with $\Delta m = \pm 1$ that give rise to an NMR signal.

1.3. Effect of an alternating magnetic field

To induce spin transitions between Zeeman eigenstates, one applies an alternating magnetic field $\mathbf{B}_1$ whose frequency matches the gap between Zeeman energy levels with $\Delta m = \pm 1$. It is usually done by irradiating the sample with a short radio-frequency (RF) pulse at $\omega_{RF} \approx \omega_0$. A linearly polarized magnetic field of the RF pulse is thought of as a sum of two circularly polarized components rotating in opposite directions, and only the component consistent with the spin precession is considered and referred to as $\mathbf{B}_1$. The effect of $\mathbf{B}_1$ on spin populations is maximum when it is applied perpendicular to $\mathbf{B}_0$. To understand that, consider the behavior of M_z, the projection of $\mathbf{M}$ on $\mathbf{B}_0 \parallel \mathbf{z}$, as a measure of the spin populations at thermal equilibrium. When $\mathbf{B}_1$ is on, the magnetization $\mathbf{M}$ precesses around the summary vector $\mathbf{B}(t) = \mathbf{B}_0 + \mathbf{B}_1(t)$, following a spiral-like trajectory. The effect of $\mathbf{B}_0$ is conveniently concealed by switching to the reference axis frame that is fixed to the $\mathbf{B}_1$ vector. In this rotating frame, the $\mathbf{M}$ vector is seen to precess around $\mathbf{B}_1$ as if it is the only effective (static) field, $\mathbf{B}_{eff} = \mathbf{B}_1$ (Fig. 4, left). Apparently, such a field has a maximum torque effect on M_z, hence on the spin population, when it is perpendicular to $\mathbf{B}_0$.

When $\omega_{RF} \neq \omega_0$, $\mathbf{B}_{eff}$ no longer coincides with $\mathbf{B}_1$ (Fig. 4, right). What is more, $\mathbf{B}_1$ is no longer in-phase with the precessing spins. Thus, the effect of the alternating magnetic field is the less the more its frequency deviates from ω_0, hence the name *resonance*. In resonance, the RF pulse of duration t_p rotates the $\mathbf{M}$ vector from $\mathbf{B}_0 \parallel \mathbf{z}$ towards the *xy*-plane by the angle

$$\alpha = \gamma B_1 t_p \tag{8}$$

Off resonance ($\omega_{RF} \neq \omega_0$), the $\mathbf{M}$ turns around the tilted effective field $\mathbf{B}_{eff} = B_1 \mathbf{e}_y + ((\omega_0 - \omega_{RF})/\gamma)\mathbf{e}_z$, staying on a cone of the semi-angle $\theta = \arctan(\gamma B_1 /(\omega_0 - \omega_{RF}))$.

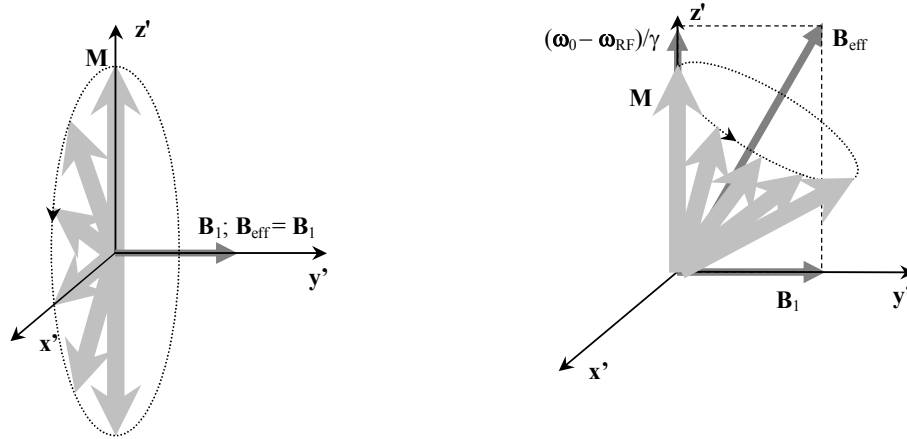*Fig. 4. Precession of $\mathbf{M}$ in the summary field $\mathbf{B} = \mathbf{B}_0 + \mathbf{B}_1$ as seen from the reference axis system x'y'z' rotating with $\mathbf{B}_1$ around $\mathbf{B}_0$ at the frequency ω_{RF}. Left: $\omega_{RF} = \omega_0$; the effective field in the x'y'z' frame is $\mathbf{B}_1$. Right: $\omega_{RF} < \omega_0$; the effective field is $\mathbf{B}_1 + (\omega_0 - \omega_{RF})/\gamma$.*

Since the Larmor frequency ω_0 corresponds to the energy split between the eigenstates that differ by $\Delta m = \pm 1$ (see Eq. 6), it is transitions between those states that are only excited by the RF pulse. For instance, despite having three Zeeman eigenstates, the spins-1 system exhibits only one NMR frequency which corresponds to the transitions $|1,-1\rangle \leftrightarrow |1,0\rangle$ and $|1,0\rangle \leftrightarrow |1,+1\rangle$, the transition $|1,-1\rangle \leftrightarrow |1,+1\rangle$ with $\Delta m = \pm 2$ being "forbidden". (Transitions with $\Delta m \neq \pm 1$ caused by molecular motion manifest themselves in spin relaxation, see Section 3.3.)

1.4. NMR signal in the time- and frequency-domain

The transversal component of the magnetization, $M_{xy}(t)$, produced by the RF pulse precesses around $\mathbf{B}_0$ and, as such, can be detected with a pickup coil. Usually, it is the same coil that generates the RF pulse. Individual spins precess with a slightly different frequencies (see Section 2) and therefore gradually get out of phase with respect to each other. As a result, the net magnetization $M_{xy}(t)$ vanishes shortly with a characteristic time constant T_2^*. The process is called free induction decay (FID). Simultaneously, the spin-lattice relaxation recovers the longitudinal component M_z back to its equilibrium value, M_0, with a time constant T_1. The overall time-dependence of $\mathbf{M}$ is given by

$$\begin{bmatrix} M_x(t) \\ M_y(t) \\ M_z(t) \end{bmatrix} = \begin{bmatrix} M_0 \sin\alpha \cos(\omega_0 t) e^{-t/T_2^*} \\ M_0 \sin\alpha \sin(\omega_0 t) e^{-t/T_2^*} \\ M_0 \cos\alpha + (1 - e^{-t/T_1})(M_0 - M_0 \cos\alpha) \end{bmatrix} \xrightarrow{\alpha = 90°} \begin{bmatrix} M_0 \cos(\omega_0 t) e^{-t/T_2^*} \\ M_0 \sin(\omega_0 t) e^{-t/T_2^*} \\ M_0(1 - e^{-t/T_1}) \end{bmatrix} \quad (9)$$

Because only a small frequency range around the Larmor frequency is of interest, the NMR signal is demodulated and filtered down to a difference (acoustic) frequency $\Omega = \omega_0 - \omega_{RF}$. Using a special demodulation technique (see Section 4.1), it is possible to detect two transversal components M_x and M_y separately. Then they are combined in the computer to give a complex FID signal

$$s(t) = M_x + iM_y \quad (10)$$

To obtain a resonance line, one converts $s(t)$ from the time-domain to the frequency-domain using the Fourier transform (FT). FT is a method of harmonic analysis which represents a signal as a series of oscillatory components (harmonics). It is defined as

$$\mathrm{FT}\{s(t)\} \equiv S(\omega) = \int_{-\infty}^{+\infty} s(t) e^{-i\omega t} dt \quad (11)$$

The FT of $s(t)$ given by (9) takes the form of two Lorentzian lines: one is in absorption mode and one in the dispersion mode (Fig. 5). NMR spectra are represented in the absorption mode. Details of the data acquisition and processing into the absorption NMR spectrum is described in Section 4.4.
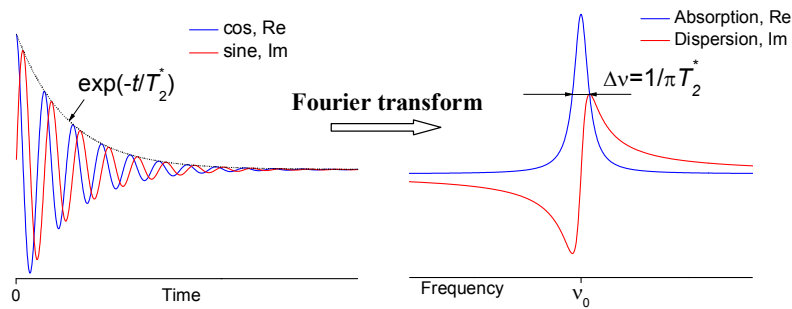
5

Fig. 5. A complex free-induction signal of frequency $v_0 = \omega_0/2\pi$ and its Fourier transform. Note the reciprocal relationship between the signal decay time T_2^* and the Lorentzian's width Δv.

1.5. Spin echoes

The FID components of different precession frequencies (so-called 'spin isochromats') can be refocused by applying the second RF pulse with a 180° flip angle (Fig. 6). The pulse will invert the spin isochromats in such a way as to make them approach each other, so that having been spread over the *xy*-plane, they eventually coalesce into one vector again (Fig. 6, e). This phenomenon is called spin echo. This technique to acquire an NMR signal is widely employed when recording the FID just after an RF pulse cannot be done without loosing an essential part of the signal due to strong self-inductance transient currents in the NMR coil (see Section 4). The spin echo acquisition is also a routine technique for spin-relaxation and diffusion measurements (see Section 3).

a: 90°-rotation **b**: de-phasing **c**: 180°-rotation **d**: re-phasing **e**: top echo
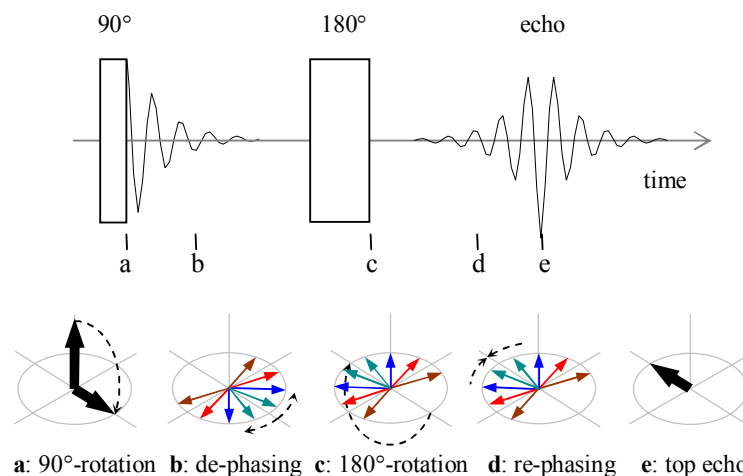
Fig. 6. Top: A spin-echo signal appears after the second (re-focusing) pulse. Bottom: The precession of spin isochromats as seen in the rotating co-ordinate system.

6

2. Spin Interactions and NMR Spectra

In molecules and crystals, the Zeeman interaction between spins and the external magnetic field is influenced by internal spin interactions which are related to the structure and the dynamics of the spin system. Consequently, an NMR signal comprises not only one Lorentzian line but many, constituting an NMR spectrum. The power of NMR spectroscopy as an analytic method relies on this influence.

2.1. Chemical shift

An exact value of the Larmor frequency in covalent compounds and ions depends on the electron distribution around the nucleus. The $\mathbf{B}_0$ field produces diamagnetic currents within electron orbitals which generate a secondary field opposing $\mathbf{B}_0$ (Fig. 7). It reduces the local field at the nucleus, hence the Larmor frequency, by a small fraction σ :

$$\omega_0 = -\gamma B_0 (1 - \sigma) \qquad (12)$$

Such a shielding effect of surrounding electrons is called chemical shift for its correlation with the chemical structure. In aromatic compounds, the diamagnetic currents may result in an opposite effect of de-shielding which enhances the local field. Besides, a local field enhancement caused by unpaired electrons takes place in paramagnetic compounds.

The chemical shift is proportional to the $\mathbf{B}_0$ field strength. To compare spectra recorded with different magnets, one measures it in relative units – parts per million (ppm), as a normalized difference between the observed NMR frequency and that in a reference compound:

$$\delta = \frac{\omega - \omega_{ref}}{\omega_{ref}} \qquad (13)$$

The standard reference in ^{1}H NMR is tetramethylsilane (TMS or SiMe$_4$). The protons in other compounds are usually less shielded compared to TMS and therefore resonate at higher frequencies (Fig. 8). Historically, NMR spectra are plotted with the chemical shift δ increasing from right to left, so goes the NMR frequency scale.

Fig. 7. Diamagnetic currents in a 1s-orbital. In covalent compounds, non-spherical electron distribution in the orbitals involved in chemical bonding makes the currents orientation dependent, resulting in chemical shift anisotropy (CSA).
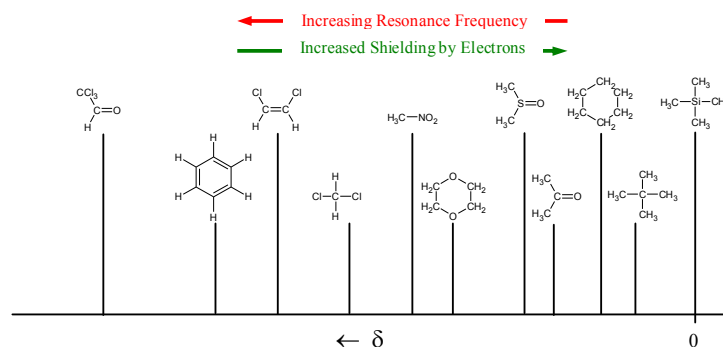

$\mathbf{B}_0$

1s – orbital

induced magnetic moment at nucleus

induced electron motion

← δ 0
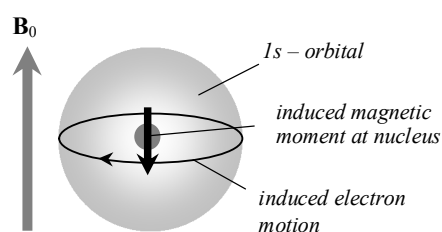
Fig. 8. Relative Larmor frequency positions of ^1H in different molecules. Resolving resonances that differ by a small fraction reveals fine details of the chemical environment.

The electron shielding effect depends on the orientation of the molecular orbitals relative to the $\mathbf{B}_0$ field. Reorientation of a molecule, or molecular segments, as well as rotation of a whole sample in the $\mathbf{B}_0$ field, change the chemical shift in general. This orientation-dependence is called a chemical shift anisotropy (CSA). If one denotes by θ the angle between the $\mathbf{B}_0$ field and a chemical bond, or a crystallographic axis, and by $\Delta\sigma$ the magnitude of CSA, then

$$\omega_{CSA} = \frac{2}{3}\gamma B_0 \Delta\sigma \times \frac{1}{2}(3\cos^2\theta - 1) \qquad (14)$$

In liquids, molecular motion averages CSA to zero, leaving only an isotropic (orientation-independent) part of the chemical shift. On the right are tabulated typical ranges of isotropic δ's for selected nuclei. The chemical shift is sensitive to the temperature and the solvent used, so one has to report that information when publishing NMR spectra.

Nucleus	δ, ppm	Standard
^{1}H	12 to −1	SiMe$_4$
^{7}Li	5 to −10	LiCl
^{13}C	240 to −10	SiMe$_4$
^{19}F	100 to −300	CFCl$_3$
^{31}P	230 to −200	H$_3$PO$_4$

2.2. Electric quadrupole coupling

Another effect of the electronic environment on NMR spectra arises from the electric interaction between the electrons and the nucleus. Nuclei of spin $I > 1/2$ (*e.g.* ^{2}H, ^{7}Li, ^{14}N, in all about 74%) have a non-spherical distribution of the electric charge giving rise to a nuclear electric quadrupole moment, Q. The latter determines the electrostatic energy of the nucleus in an electric field gradient, $\mathbf{V}$, produced by surrounding charges. The energy depends on the orientation of the quadrupole relative to $\mathbf{V}$ (Fig. 9).

Fig 9. A quadrupole nucleus in an electric field gradient by four external charges. The quadrupole energy in case (a) is less than in case (b).

8
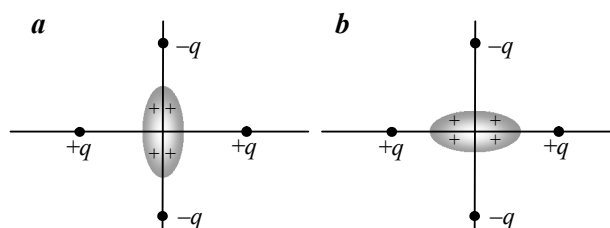
In a strong $\mathbf{B}_0$ field, the orientation of the nucleus is quantized according to the magnetic quantum number m. The quadrupole interaction must therefore affect respective Zeeman eigenstates, $|I,m\rangle$, shifting their energy levels as depicted in Fig. 10. Note that the levels with $+m$ and $-m$ are shifted in the same direction, as the quadrupole energy is invariant to the nucleus inversion. The NMR transitions with $\Delta m = \pm 1$ between so-shifted levels yield $2I$ resonance lines (Fig. 10, in middle).
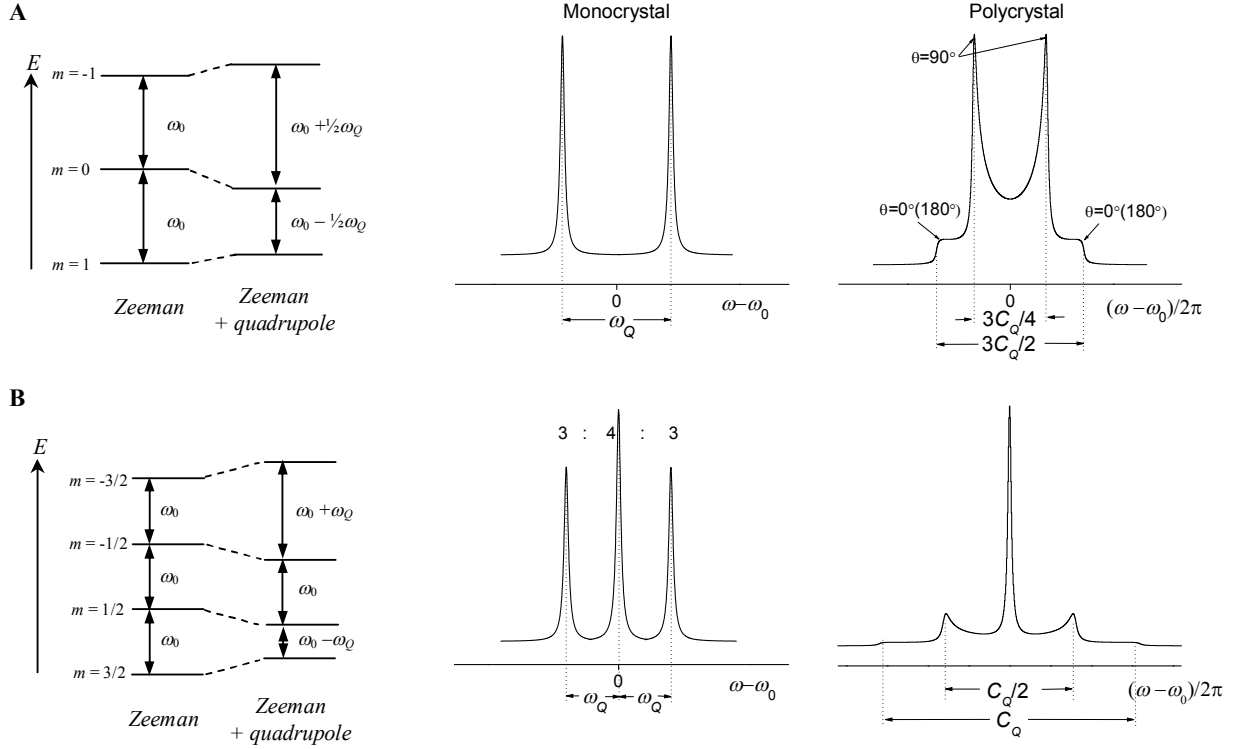

Fig. 10. Energy levels for spin-1 (A) and spin-3/2 (B) systems and corresponding mono- and poly-crystal spectra. The central transition frequency of spins-3/2 does not depend, in the first order, on the molecule orientation angle θ, so that the central peak stays sharp in poly-crystal spectra.

The multiplicity of a quadrupole spectrum should not be taken as if there are multiple Larmor frequencies in the quadrupole spin systems. Indeed, the precession of $\mathbf{M}$ is determined by the local magnetic field strength (recall Eq. (3)) and, as such, must not be changing upon electric interactions. What changes is the length of M_{xy} which oscillates during precession in response to coherent spin transitions between the eigenstates. Nevertheless, one can think of such an oscillatory M_{xy} as a sum of, say, two sub-components for the case of $I = 1$, precessing in the rotating frame in opposite directions with the frequencies $\pm\frac{1}{2}\omega_Q$, hence two resonance lines.

The line splitting ω_Q is determined by the quadrupole coupling constant C_Q,

$$C_Q = e^2 qQ/h \text{ (in Hz)} \qquad (15)$$

which depends on the quadrupole moment Q (a nuclear property) and the electric field gradient's

9

principle value *eq* (a molecular property). C_Q values for selected spin systems can be found in the literature (see Further Reading). Since electric field gradient is fixed to a chemical bond, the rotation of the bond by the angle θ relative to the $\mathbf{B}_0$ field (which specifies the nuclear polarization) changes ω_Q as

$$\omega_Q = \frac{3\pi C_Q}{I(2I-1)} \times \frac{1}{2}(3\cos^2\theta - 1) \qquad (16)$$

Polycrystalline samples, or powders, where all orientation with θ in [0, 90°] are present, exhibit continuous NMR spectra of the shapes reflecting the orientation probability (Fig. 10, on the right).

2.3. Dipole-dipole coupling

So far we have been considering interactions between individual spins and their electronic environment. Spins are also coupled with one another through their magnetic fields, alike tiny magnet bars or magnetic dipoles (Fig. 11). The magnetic dipole-dipole coupling depends on the distance between the spins ($\propto r^{-3}$) and their mutual orientation (Fig. 12). The dependence on the distance is accounted for in a dipole-dipole coupling constant:

$$C_D = -\frac{\mu_0}{4\pi}\frac{\gamma_j\gamma_k\hbar}{r_{jk}^3} \text{ (in rad/s)} \qquad (17)$$
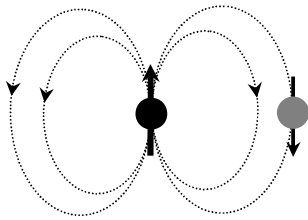

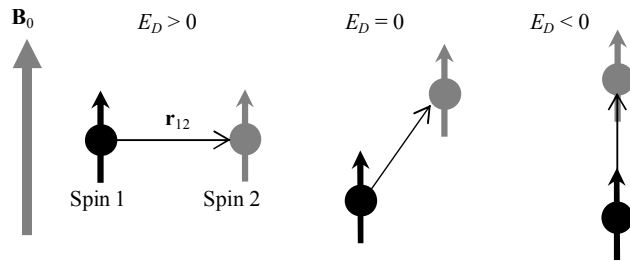*Fig. 11. One nuclear dipole in the magnetic field by the other.*

Fig. 12. The orientation dependence of the interaction energy of two magnetic dipoles in a strong $\mathbf{B}_0$ field.

The effect of dipole-dipole coupling on the NMR spectrum appears different for homonuclear pairs (like ^1H-^1H, ^{19}F-^{19}F) and heteronuclear pairs (like ^{13}C-^1H, ^{31}P-^6Li). Consider first weakly-coupled homonuclear spin-1/2 pairs, *e.g.* protons. A spin pair is taken as a single quantum system and, as such, is described by one set of eigenstates called Zeeman product states, $|\alpha\alpha\rangle$, $|\alpha\beta\rangle$, $|\beta\alpha\rangle$ and $|\beta\beta\rangle$. Without dipole-dipole coupling, the product states would represent stationary states. The coupling makes the states $|\alpha\beta\rangle$ and $|\beta\alpha\rangle$ be unstable (enabling so-called flip-flop spin transitions between them) and results in a new set of stationary states $|S\rangle$ and $|T_M\rangle$ (Fig. 13). The states $|T_M\rangle$ correspond to the total angular momentum $I = 1$, with respective total $M = 1, 0, -1$, and are called triplet states of a spin pair. The state $|S\rangle$ corresponds to $I = 0$ and is called a singlet state. Since the total angular momentum must not

change under an RF pulse, NMR transitions are observed between the triplet states only (see arrows in Fig. 13). It yields a doublet, as shown in Fig. 13. The line splitting ω_D in the doublet is

$$\omega_D = 3C_D \times \frac{1}{2}(3\cos^2\theta - 1) \qquad (18)$$

where θ is the angle between $\mathbf{r}_{12}$ and $\mathbf{B}_0$.
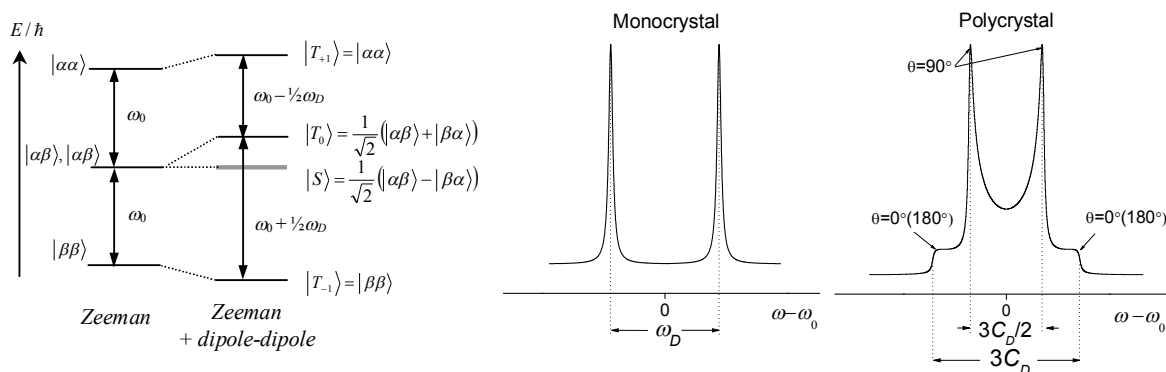

Fig. 13. Energy levels of weakly-coupled homonuclear spin-1/2 pairs and their dipolar spectra. Note the total resemblance of these spectra to the quadrupolar spectra of spins-1 in Fig. 10A.

The complexity of the dipolar spectrum of homonuclear spins increases rapidly with their number. The spectrum of three equivalent spins-1/2 (*e.g.* protons in a CH_3 group) comprises already nine lines. For multi-spin systems, one usually observes one broad line made up of many unresolved resonances.

Heteronuclear spin pairs (^{13}C-^1H, ^{13}C-^{19}F, ^1H-^2H, etc.) for which the difference in Larmor frequencies is much greater than the coupling constant C_D, can be with a good accuracy represented by Zeeman product states as stationary states. For comparison, a ^{13}C-^1H pair with the bond length $r_{12} = 0.11$ nm has $C_D = 2\pi \times (23 \text{ kHz})$, while the difference in the Larmor frequencies of ^{13}C and ^1H in the typical magnetic field of 7 T is $2\pi \times (225 \text{ MHz})$, that is ten times greater. Such pairs produce so-called first-order spectra which are considered in the next section (see Fig. 15).

Due to its strong distance dependence ($\propto 1/r^3$), the dipole-dipole coupling can be used to ascertain the spatial arrangement of spins within a molecule, either from the line shape analysis of solid-state powder spectra or by measuring the nuclear Overhauser effect in solutions (see Further Reading).

2.4. *J*-coupling

In addition to the direct, through-space dipole-dipole interaction, spins are coupled via electron shells along chemical bonds. The magnetic moment of one nucleus polarizes spins of the bonding electrons which in turn affects the other nucleus (Fig. 14). Such a through-bond dipole-dipole interaction is called *J*-coupling. The magnitude of *J*-coupling is controlled by the coupling constant *J* which depends on the bond length and the bond angle.

J-coupling varies with the molecular orientation relative to the $\mathbf{B}_0$ field, alike the direct dipolar interaction, but it does not average to zero under molecular reorientation. The residual, isotropic, part of *J*-coupling is called scalar coupling, and usually it is only this part that can be measured from NMR spectra. It is proportional to a scalar product of magnetic moments of the coupled spins, $\mu_1\mu_2$.

Fig. 14. Proton-proton J-coupling via two C-H bonds.

The scalar coupling is much weaker than the direct dipolar interaction (Fig. 17) and as such cannot be observed unless the latter interaction is averaged out, as *e.g.* in liquids (see Section 3.1).

The effect of the scalar coupling on the NMR spectrum depends on whether the coupled spins are magnetically equivalent (having the same chemical shift) or not. Consider first the system of two equivalent spins-1/2 which they call A_2 system. It has four eigenstates $|T_M\rangle$ and $|S\rangle$, same as for the direct dipolar coupling (Fig. 13) but with the triplet energy levels $|T_M\rangle$ now being all equally shifted. The shift is given by the projection of the spins on one another given by the product $\mu_1\mu_2$. The NMR transitions between the triplet states produce in such a case only one resonance line at the chemical shift frequency. Thus, the scalar coupling between magnetically equivalent spins does not manifest itself in the spectrum. (Note that the direct dipole-dipole coupling within an equivalent group is observed.)

Consider next two magnetically non-equivalent spins-1/2 whose difference in chemical shifts is much greater than a scalar coupling magnitude (so-called AX system). Appropriate eigenstates for the AX system are the Zeeman product states whose energy levels are now shifted depending on the individual spins' polarization in the $\mathbf{B}_0$ field rather than on $\mu_1\mu_2$, according to the formula:

$$E = J m_A m_X \text{ (in Hz)} \tag{19}$$

NMR transitions in the AX system occur separately for spins A and X, hence it is either m_A or m_X that changes at a time. Taking that into account, one obtains the AX spectrum with individual spins' resonances being split in doublets by *J* Hz each (Fig. 15).

Spectra of spin systems in which the difference in chemical shift are much greater than coupling constants are called first-order spectra. They allow for a simple interpretation based on the idea of a local field exerted by spin A on spin X that takes on $2I+1$ orientations, thus resulting in $2I+1$ lines in the X-multiplet, and vice versa. In general, *n* equivalent spins-*I* split a neighbor's resonance to $2In+1$ lines, with the intensity ratios following a binomial distribution (Fig. 16). To get relatively simple first-order spectra is one of the reasons of using strong $\mathbf{B}_0$ fields (recall that the chemical shift scales with $\mathbf{B}_0$).
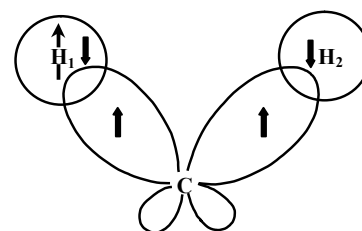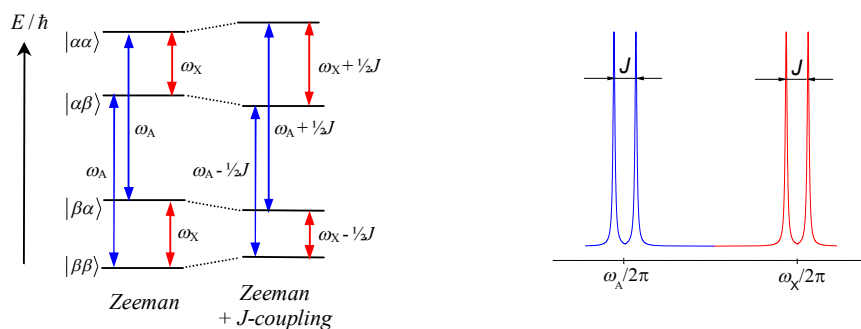
Fig. 15. Energy levels of an AX system in the presence of J-coupling (left) and the corresponding first-order spectrum (right).

The effect of the heteronuclear *J*-coupling on the observed nuclei can be annulled by irradiating the neighboring spins at their resonance frequency. It is used, for example, in ^{13}C NMR spectroscopy for "decoupling" of ^{1}H spins from the observed ^{13}C spins. The heteronuclear *J*-splitting also vanishes when the neighboring spins have a short spin-lattice relaxation time T_1.

Fig. 16. A first-order ^{1}H NMR spectrum of ethanol in CDCl$_3$, at $\omega_0 = 2\pi \times 90$ MHz. The protons in CH$_3$ and CH$_2$ groups are J-coupled to each other resulting in a triplet and a quartet, respectively, split by 7 Hz each. The OH-group's proton is remote from the others and appears as a singlet.
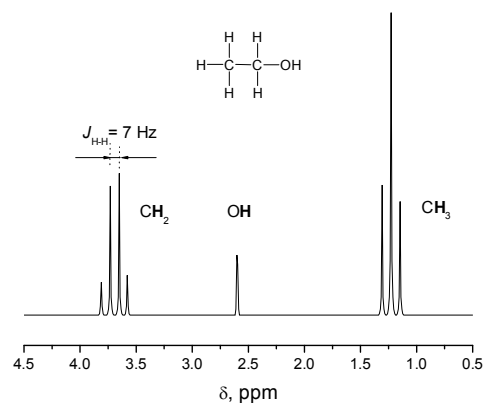
Table 2. Magnitude of J-coupling for some spin pairs.

Spin pair	^{1}H -^{1}H	^{1}H -^{13}C	^{19}F -^{19}F	^{19}F -^{1}H	^{19}F -^{31}P	^{19}F -^{13}C	^{31}P-^{1}H	^{31}P-^{31}P
Max. *J*, Hz	18	320	370	96	1400	240	700	500

2.5. Anisotropy of spin interactions

Interesting enough, different spin interactions – CSA, quadrupole coupling and dipole-dipole coupling, exhibit alike dependence on the molecular orientation in the $\mathbf{B}_0$ field (see Eqs. 14, 16, 18). It follows from a tensor character of those interactions: they all involve variables that behave as tensors under rotation. Consider for example the dipole-dipole coupling. As seen from Fig. 11, the dipolar energy depends on the projection of two momentum vectors, $\boldsymbol{\mu}_1$ and $\boldsymbol{\mu}_2$, on a connection vector $\mathbf{r}_{12}$. The expression for it must therefore include a matrix product that implements such a projection. The

corresponding matrix's elements (a tensor of rank 2) depend on the vectors' orientation the way defined by tensor algebra, which would be common for all interactions.

Proceeding with this example, the momentum vectors $\boldsymbol{\mu}_1$ and $\boldsymbol{\mu}_2$ are polarized along the $\mathbf{B}_0$ field, $\mathbf{B}_0 \parallel \mathbf{e}_z$, and in a strong enough field (>1 T), it is only z-projection of $\boldsymbol{\mu}$ that matters. To find the dipolar energy, one has to express μ_z defined in the laboratory frame (LF) through its components in the frame fixed to $\mathbf{r}_{12}$. The latter is naturally chosen with z-axis along $\mathbf{r}_{12}$ and called principle axis system or PAS. Hence,

$$\mu_x^{\mathrm{PAS}} = \mu_z^{\mathrm{LF}} \cos\varphi \sin\theta\,; \quad \mu_y^{\mathrm{PAS}} = \mu_z^{\mathrm{LF}} \sin\varphi \sin\theta\,; \quad \mu_z^{\mathrm{PAS}} = \mu_z^{\mathrm{LF}} \cos\theta \tag{20}$$

where (θ, φ) are the polar angles of $\mathbf{e}_z$ in PAS. Expressing the momentum vectors through their PAS components enables one to write the dipolar energy, hence the dipolar splitting ω_D, via the scalar product

$$\omega_D \propto \sum_\alpha \mu_{1\alpha}^{\mathrm{PAS}} D_{\alpha\alpha}^{\mathrm{PAS}} \mu_{2\alpha}^{\mathrm{PAS}} \propto D_{xx}^{\mathrm{PAS}}(\cos\varphi \sin\theta)^2 + D_{yy}^{\mathrm{PAS}}(\sin\varphi \sin\theta)^2 + D_{zz}^{\mathrm{PAS}}(\cos\theta)^2 \tag{21}$$

The coefficients $D_{\alpha\alpha}^{\mathrm{PAS}}$ are called principle values of the dipolar interaction tensor. The latter is axially symmetric, $D_{xx}^{\mathrm{PAS}} = D_{yy}^{\mathrm{PAS}}$, reflecting the invariance of the dipolar energy under simultaneous rotation of $\boldsymbol{\mu}_1$ and $\boldsymbol{\mu}_2$ around $\mathbf{r}_{12}$. Moreover, $\sum_\alpha D_{\alpha\alpha}^{\mathrm{PAS}} = 0$, which gives after some trigonometry

$$\omega_D(\theta) \propto \frac{1}{2}(3\cos^2\theta - 1) \tag{22}$$

Expressions like Eq. (21) exist for CSA and quadrupole coupling too, with respective interaction tensor components entering. Only those interactions are axially asymmetric in general, so that the orientation dependence of ω_{CSA} and ω_Q may not be as simple as Eq. (22) but also include the azimuthal angle φ. Anisotropic lineshape analysis is widely used in molecular dynamics studies (see next Section 3).
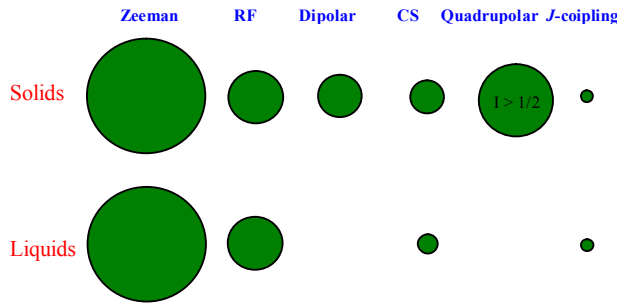

Fig. 17. The rough relative effect of spin interactions on NMR spectra.

3. Motion Effects in NMR

3.1. Motional averaging of spin interactions

The frequency distribution due to the orientation dependence of spin interactions averages out under molecular reorientation, provided that: (i) the reorientation is fast on an NMR time scale and (ii) it is isotropic, meaning the angle θ takes on all values within [0, 90°] randomly. The NMR time scale is defined by the time required for different frequency components to spread by ~1 rad, such that most of the FID signal vanishes. For the spectrum extended over $\Delta\omega$ rad/s, this time is $1/\Delta\omega$ s. The above two conditions are readily met in liquids, where molecules re-orientate isotropically and with short correlation times τ_c (< 1 μs). NMR spectra of liquids collapse to sharp Lorentzian lines situated at the centers of gravity of present spin interactions. The dipole-dipole and quadrupole interactions have no isotropic parts (zero center of gravity) and, as such, do not manifest themselves in liquids' NMR spectra. What is left is isotropic chemical shifts and the splitting by the scalar coupling (see Fig. 16).

An example of the motional narrowing in solids is given in Fig. 18. It shows ^{31}P spectra of solid white phosphorus recorded at room temperature and at 25 K. White phosphorus comprises P_4 molecules that undergo rotational jumps between tetrahedral positions (related to each other by cubic symmetry). Such a high-symmetry motion effectively averages out the chemical shift anisotropy.
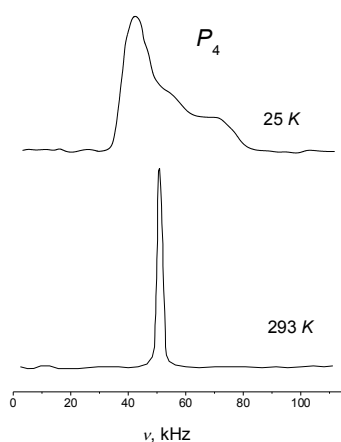
Fig. 18. [31]P spectra of solid white phosphorus at $B_0 =$ 5.6 T. The spectrum at 25 K shows powder chemical shifts over 37 kHz. The spectrum is additionally broaden by [31]P-^{31}P dipolar coupling of 2.5 kHz in magnitude. At 293 K, the chemical shifts distribution is averaged out by rapid reorientation of P_4 molecules [from Chem. Phys. 6 (1974), 226-234].

When the molecular motion is fast ($\tau_c < 1/\Delta\omega$) but anisotropic, as *e.g.* in liquid crystals, the spin interactions retain the orientation dependence given by Eq. (21) but with reduced (partially averaged) tensor components. The tensor reduction is determined by the geometry of motion. Fig. 19c shows quadrupolar ^{2}H NMR spectra of an aromatic molecule undergoing two unlike anisotropic reorientation: 180° flip-flops and 60°-step jumps on the ring plane. One can see that the spectra average quite differently in those two cases. The intermediate regime between slow and fast motion, $\tau_c \sim 1/\Delta\omega$, is where the spectra are affected most dramatically. The individual frequency components gather under such an intermediate motion unusual widths and phases, yielding rich patterns (Fig. 19b).

3.2. Chemical exchange and NMR spectrum

An atom or an ion may exchange between chemically non-equivalent sites (*e.g.* in the course of a chemical reaction), so that the tagged nucleus experience various chemical shifts during a free-induction decay. The effect of the chemical exchange on the spectrum depends on the relation between the exchange rate k_{ex} and the frequency difference $\Delta\omega$. To observe two distinctive frequencies with the gap $\Delta\omega$ requires that the corresponding FID components have gained a significant phase shift before the frequencies change. The phase shift over period $\tau_{ex} = 1/k_{ex}$ is $2\pi\Delta\omega \times \tau_{ex}$, meaning that one can only distinguish frequencies when $2\pi\Delta\omega \times \tau_{ex} \gg 1$ rad, or $k_{ex} \ll \Delta\omega$ (the condition for slow exchange). This is illustrated in Fig. 20 where protons in two N-methyl groups in a derivative of azapropazone are in the slow exchange regime at $T = 223$ K. As the temperature increases and k_{ex} approaches $\Delta\omega$, individual resonances first broaden, then coalesce and, when $k_{ex} \gg \Delta\omega$ (the condition for fast exchange), they sharpen into a single average peak.

Measuring the spectrum under chemical exchange allows to estimate chemical reaction rates under equilibrium conditions which are hardly accessible otherwise. It also finds a use in studies of ionic diffusion in crystalline and glassy ion conductors.
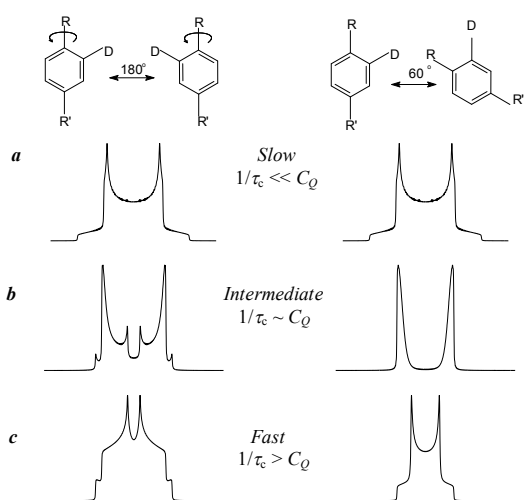
Fig. 19. Powder deuterium NMR spectra of an aromatic molecule jumping by 180° around C_2-axis and by 60° on a ring plane, at different rates compared to a static spectrum width.
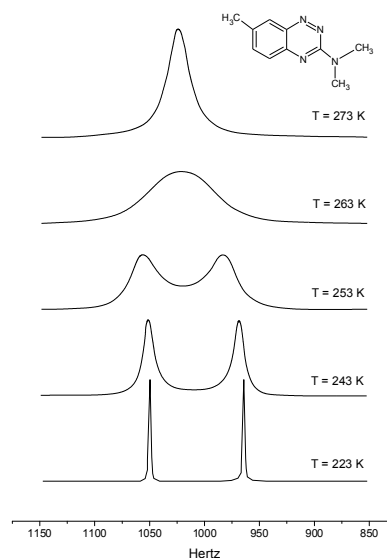
Fig. 20. ^1H NMR spectra of the N-methyl groups in a derivative of azapropazone. The lines of two equally populated sites under exchange coalesce when $k_{ex} = 0.35 \times \Delta\omega$, see the spectrum at 263 K [from Prog. NMR Spec. 43 (2003) 63–103].

3.3. Spin relaxation

The disturbance of spin interactions by thermal motion induces spin transitions and eventually brings the spin state population to its thermal equilibrium. The transitions' probability is proportional to a fluctuation part of spin interactions squared. The process is called the spin-lattice relaxation, or T_1-relaxation, the term 'lattice' standing for thermal molecular environment.

These motion-induced transitions have much in common with the effect of the applied RF field, including its resonance character: the efficiency of the motional disturbance depends on how much of it occurs at the spin resonance frequency. To illustrate that, consider a simple case of uncoupled spins-1/2 diffusing among sites with different local field B_y. The Zeeman interaction fluctuates randomly with B_y. To describe this process in terms of frequency, one introduces a spectral density function $J(\omega)$, as a Fourier transform of a fluctuation correlation function $C(t)$ (Fig. 21). The T_1-relaxation rate is then expressed as a product of the mean-square magnitude of the fluctuating Zeeman interaction, $\gamma^2 \left\langle B_y^2 \right\rangle$, and the spectral density at the spin resonance frequency ω_0:

$$1/T_1 = \gamma^2 \left\langle B_y^2 \right\rangle J(\omega_0) \qquad (23)$$

The actual form of $J(\omega_0)$ will depend on the details of the motional process. Hence, for isotropic diffusion, $C(t)$ is an exponentially decaying function,

$$C(t) = \left\langle B_y^2 \right\rangle \mathrm{e}^{-t/\tau_c} \qquad (24)$$

and $J(\omega)$ takes in this case the form of a Lorentzian:

$$J(\omega) \propto \frac{\tau_c}{1+\omega^2\tau_c^2} \qquad (25)$$

The spectral density (25) expressed at the resonance frequency ω_0 goes through maximum when $\tau_c = 1/\omega_0$, so does the rate of T_1-relaxation (Fig. 22).
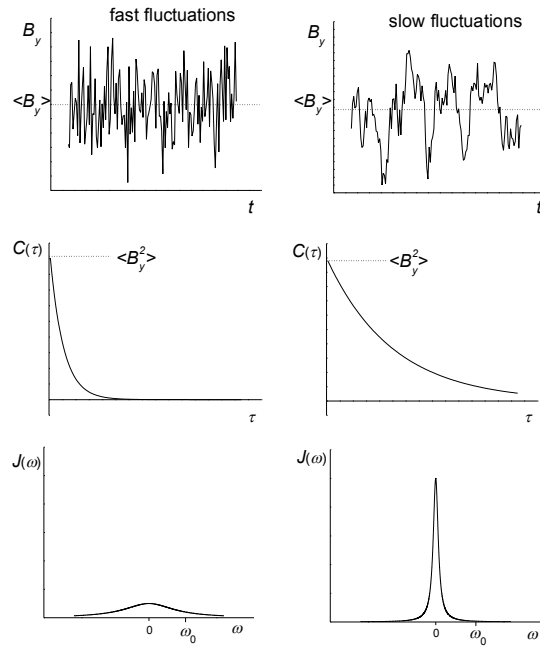
Fig. 21. Correlation function $C(\tau)$ and spectral density $J(\omega)$ of fast and slow fluctuations.

A particular mechanism of T_1-relaxation is determined by a predominant spin interaction. In other words, the effect of molecular motion depends on what interaction it modulates. Note that the fluctuation of dipole-dipole and quadrupole interactions might have a (great) effect on T_1-relaxation even when they are not visible in the NMR spectrum.

Measuring spin-lattice relaxation rates gives valuable information on molecular dynamics (correlation times, activation energies, the geometry of motion); it is also employed for studying

molecular structure through the nuclear Overhauser effect in dipole-coupled spin systems (see Further Reading). To measure T_1, one first disturbs the equilibrium spin magnetization by inverting it with a 180° RF pulse or completely destroys it with a saturation pulse train. Then, an FID signal is recorded in a variable delay τ to monitor the recovery of M_z toward equilibrium (hence the other name 'longitudinal relaxation'). The recovery curve is fitted with the functions:

$$M_z(\tau) = M_z^{eq}(1 - 2e^{-\tau/T_1}) \quad \text{inversion-recovery} \qquad (26)$$

$$M_z(\tau) = M_z^{eq}(1 - e^{-\tau/T_1}) \quad \text{saturation-recovery} \qquad (27)$$

which gives the sought-after T_1 value.

Another type of spin relaxation is spin-spin or T_2-relaxation. It describes the diminution of phase coherence of precessing spin isochromats because of random changes of the local longitudinal magnetic field. This causes a irrevocable loss of the transverse net magnetization with a characteristic time T_2 (hence another name 'transverse relaxation'). One mechanism of T_2-relaxation is individual spin transitions in the course of T_1-relaxation, as the latter is accompanied by individual spin's re-orientation which changes the longitudinal field at neighboring spins in a random fashion. Mutual flip-flop transitions of two coupled spins have similar effect. Another factor influencing T_2-relaxation is molecular diffusion in a static but inhomogeneous magnetic field. The two latter mechanisms of T_2-relaxation are independent on the NMR frequency but controlled by the correlation time and the geometry of motion.

Spin-spin relaxation time T_2 is measured from the decay of a spin-echo amplitude as the inter-pulse delay is varied (see Section 1.5). The so-measured T_2 must not be mixed up with the FID time T_2^*. The free-induction decay is affected by both molecular motion (dynamic part) and the resonance frequency distribution (static part). The latter is reversed in a spin-echo experiment whereas the former is irreversible, which means $T_2 \geq T_2^*$.

Fig. 22. Dependence of T_1 and T_2 on the motional correlation time τ_c. The relation $T_1 \geq T_2 \geq T_2^*$ holds.

18
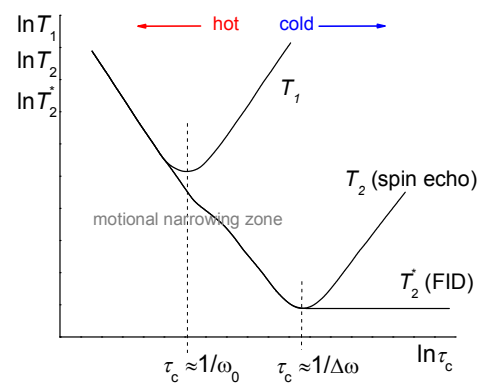
4. The NMR Experiment

4.1. Fourier-transform NMR spectroscopy

In early days of NMR spectroscopy, the NMR signal was recorded directly in the frequency-domain. The NMR sample was irradiated by a continuous RF wave near ω_0 while the $\mathbf{B}_0$ field was swept to meet a resonance condition. The spin system was interrogated in a sequential manner, with one resonance frequency at a time. This technique is known as the continuous-wave NMR spectroscopy (CW-NMR). In its Fourier transform counterpart (FT-NMR), one applies a short RF pulse to excite all resonance frequencies at once. The response of the spin system to the pulse is recorded as a function of time – an FID signal, which is then transformed to a frequency spectrum by means of FT. This approach provides a better signal-to-noise ratio (SNR) compared to CW-NMR. In practice, it means faster measurements. The gain in SNR is the greater, the wider the spectrum and the narrower separate lines. Apart from that, the FT-NMR enables manipulation of spins through a series of pulses with specified delays (pulse sequences) to get extra information on the molecular dynamics and structure (see Further Reading).

The frequency bandwidth excited by the RF pulse of duration t_p is $\sim 1/t_p$ Hz. Hence, the broader the spectrum, the shorter RF pulse is required for its uniform excitation. The resonance frequencies are measured relative to the pulse carrier ω_{RF}, as they are seen in the rotating frame, $\Omega = \omega - \omega_{RF}$, and the carrier frequency is usually set at the middle of the spectrum. The latter minimizes the required excitation bandwidth and reduces the noise. In return, it introduces the problem of discrimination between positive and negative Ω's. This problem is solved by means of a quadrature detection technique: The FID signal is split into two channels – `Re` and `Im`, where it is mixed with reference signals of the same frequency ω_{RF} but 90°-shifted phases. This makes two demodulated signals proportional to cosine (M_x) and sine (M_y) projections of the precessing magnetization. Knowing how either projection changes in time, one can ascertain the direction of precession in the rotating frame, hence the right sign of Ω. Having both projections also allows of getting a spectrum in the form of absorption Lorentzians (see Section 1.4). The demodulated `Re` and `Im` signals get digitized in ADC's, and their digital representatives are stored in separate computer's memory blocks as a complex signal $s(t_i)$. For unambiguous representation of all spectral components in $s(t_i)$, the digitization rate must be no less than the spectrum width, $1/\Delta t \geq \Delta\Omega$.

The quadrature detection is subjected to misbalancing of the `Re` and `Im` channels (gain mismatch, phase shift error, direct current offsets). To eliminate related artifacts, the FID signal is accumulated in several scans with cosine and sine projections being redirected between the channels. It is achieved by switching the pulse carrier's phase in a cycle between 0°, 90°, 180° and 270°. After each of those scans cosine and sine data are routed to proper memory blocks to match up previously collected data (the 'data routing' procedure).

It is often required to accumulate many NMR signals because of a poor SNR. Accumulating in N

scans increases SNR by $\sqrt{N}$. The principle instrumental factor influencing SNR is the external magnetic field strength (NMR signal $\propto B_0^2$). SNR also depends on the quality factor (Q-factor) of the NMR probe (SNR $\propto \sqrt{Q}$) and the transmitted RF power. Material-related factors of SNR are the gyromagnetic ratio γ (NMR signal $\propto \gamma^3$) and the natural abundance of the nucleus under study.

4.2. The FT-NMR spectrometer

The transmitter tract of FT-NMR spectrometer (Fig. 23) comprises a frequency synthesizer, a pulse programmer and an RF amplifier. The role of the pulse programmer is to cut a continuous RF wave generated by the frequency synthesizer into pulses and to control the frequency and the phase of the pulse carrier and the reference signal needed for detection. The RF pulses are amplified and delivered through the duplexer to the NMR probe. The duplexer decouples transmitter and receiver tracts by blocking high-power RF pulses from entering the receiver, thus preventing it from damage. A low-power NMR signal goes to a receiver's preamplifier and then is demodulated in the quadrature detector. The demodulated signal is run through a low-pass filter to remove components laying outside spectrum including high-frequency noise. Resulting `Re` and `Im` signals of the acoustic frequency Ω are digitized in ADC's and are stored on the computer.

The NMR probe contains a LC resonant circuit tunable to the Larmor frequency of the observed nuclei, connected to the outer network through either an inductive or capacitive voltage division scheme for impedance matching. Tuning and matching capacitors are shown in Fig. 23 as C_T and C_M. The NMR coil is made in various forms – solenoid, Helmholtz coil, birdcage coil, surface coil, depending on a particular application and experimental setup.

Modern superconductive NMR magnets provide $\mathbf{B}_0$ fields up to 22 T (^{1}H Larmor frequency 900 MHz). The field is produced by tens of amps of current circulating in a superconducting coil immersed in liquid helium (Fig. 23). The helium tank is surrounded by a liquid nitrogen tank for better thermal isolation from the ambient. The NMR probe sits inside the magnet's bore along an additional set of coils, called room-temperature shim coils. They generate an extra, relatively weak magnetic field such as to compensate the main field's inhomogeneity and provide as uniform resonance conditions over the sample as possible. The $\mathbf{B}_0$ field may drift, making the resonance conditions time-dependent. High-resolution NMR spectrometers are equipped with a field-locking system which adjusts the current in the shim coils in response to the $\mathbf{B}_0$ field's drift.
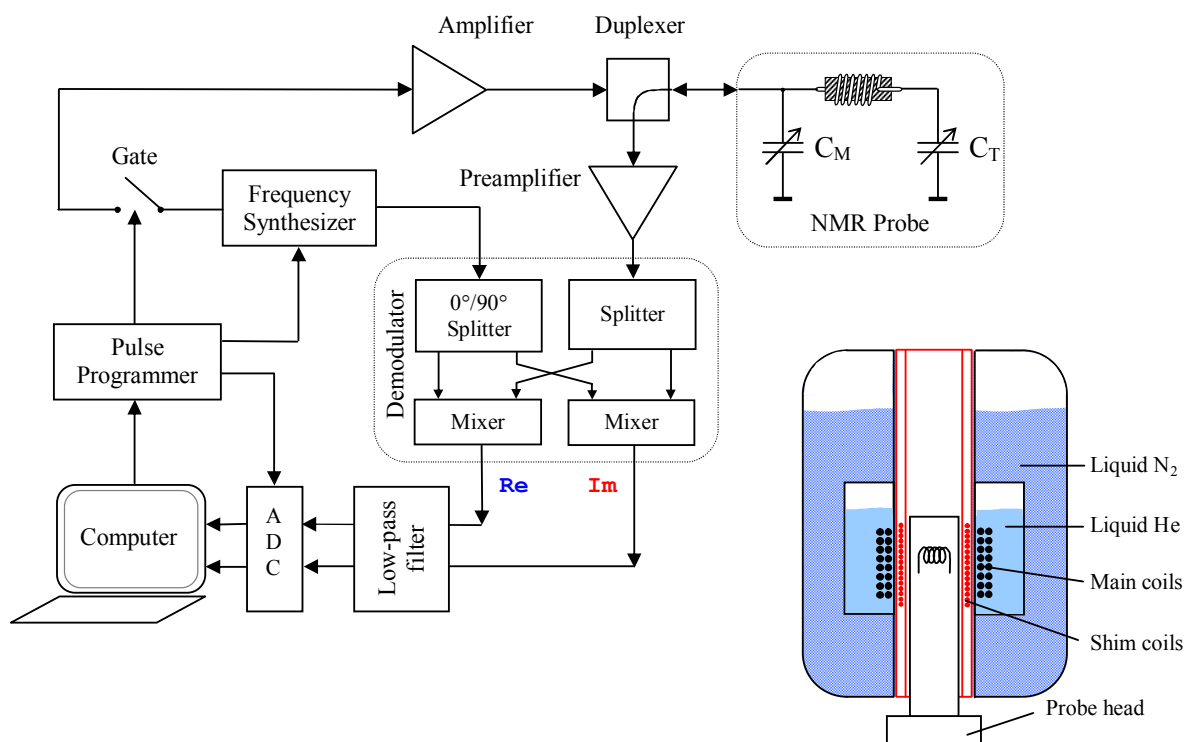
Fig. 23. FT-NMR spectrometer and a magnet.

4.3. The basic one-pulse experiment

The basic pulse-acquire experiment (Fig. 24) has the following setups.

Fig. 24. The pulse-acquire experiment.

90°-pulse length, P90. This parameter specifies the pulse duration providing a 90°-rotation of **M** at a given RF power. To optimize P90, one measures the FID magnitude varying P90 and looking at which P90 it attains its maximum.

Pulse carrier frequency, SF. SF is to be set at the middle of the NMR spectrum. The relative position of SF in the spectrum is marked by a tiny artificial signal at the center of a spectral window, owing to a non-perfect quadrature detection (a 'central-frequency' artifact).

Pulse repetition delay, RD. The most part of *z*-magnetization is recovered after the RF pulse within 3-5 T_1 seconds. Setting RD to this value maximizes SNR after a single scan, but ultimately elongates the whole (multi-scan) experiment. To maximize SNR per unit time, one sets RD to 1.3 T_1 when using a 90° pulse. Knowing the 90°-pulse length and the spin-lattice relaxation time T_1, one can also calculate the pulse duration for the Ernst angle, α_E, which is the optimum angle to obtain the maximum SNR for a given RD. The formula is $\cos\alpha_E = \exp(-RD/T_1)$. Setting RD shorter than 3-5 T_1 requires applying a couple of dummy scans before starting an actual data acquisition to let the

magnetization approach a dynamic equilibrium.

Spectral window, SW. This parameter specifies a sampling rate of the NMR signal for the ADC card. The sampling rate defines the maximum dete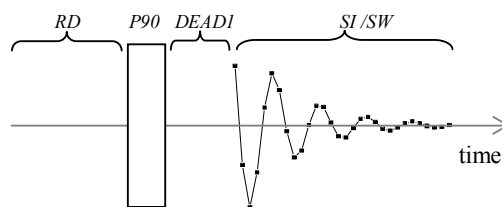ctable spectral frequency and therefore has to match the actual spectrum width $\Delta\Omega$. If SW is set narrower than $\Delta\Omega$, the spectral components lying beyond SW and not having been filtered out prior to sampling will fold into SW, mixing up with the other peaks.

Number of acquisition points, SI. This parameter defines a spectral digital resolution. It is to be set such as to sample the signal well down to the noise level. A deficient SI results in a truncated FID signal with a characteristic resonance line distortion in the form of wiggles. An excessive SI results in spending time collecting noise, which downgrades SNR. A good practice seems to be to allocate 2/3 of the acquisition time for the signal and the rest 1/3 for the noise. To benefit from using the Fast Fourier Transform (FFT) algorithm, SI has to be a power of two (*e.g.* 512, 1024, 2048, etc).

Receiver dead time, DEAD1. Switching off the RF power induces an electromotive force in the NMR coil (the self-induction effect), which overrides the FID signal for the period of time called the receiver dead time. It usually ranges from several µs to tens of µs, depending on the coil's Q-factor. Setting DEAD1 too short manifests itself as strong, clipped oscillations preceding the FID signal.

4.4. Signal processing

Prior to FT, one often doubles the dimension of the sampled FID signal, $s(t_i)$, appending zero points. This trick, called zero-filling, allows to increase spectral digital resolution without introducing noise, as it would had the points been added by elongating the acquisition time. The zero-filling is usually followed by the routine called apodization. The latter means multiplication of $s(t_i)$ by an appropriate weighting function to emphasize an initial part of FID compared to its noise-dominated tail in order to increase SNR. One example of such a weighting function is the exponential decay function. The apodization is accompanied by a line broadening. Hence, one has to find a compromise between the enhancing SNR and spoiling the spectral resolution with apodization.

FT of the complex FID signal $s(t_i)$ as a sum of cosine and sine terms is supposed to result in the complex spectrum $S(\Omega_i)$ with `Re` and `Im` components being in the form of absorption and dispersion lines, respectively (see Eq. (10) and Fig. 5). In practice, it might not be so for several reasons. First, the reference signal for the quadrature detection might be out of phase relative to the pulse carrier (*e.g.* due to a phase shift acquired in communication cables). In this case, the data collected from the `Re` and `Im` channels would be linear combinations of cosine and sine projections of $\mathbf{M}(t)$. Consequently, the spectral `Re` and `Im` components would be linear combinations of the absorption and dispersion lines. The phase mismatch can be corrected after FT rotating the entire dataset $S(\Omega_i)$ by a certain angle until the `Re` component starts looking like an absorption line. This stage of processing is called zero-order phase correction; in practice, it is applied looking at the most intensive peak, no matter what happens to others.

The phase error depends on the position Ω of the peak. When $\Omega \neq 0$, the **M** vector rotates around the tilted effective field **B**$_{eff}$ (see Section 1.4) so that its projection on the *xy*-plane after a 90°-pulse is shifted from the *x*-axis by the angle $\propto \Omega / \gamma B_1$. Another contribution to the frequency-dependent phase shift is due to the receiver dead time. The later start of FID acquisition effectively displaces a time scale origin. In terms of FT, this means a phase shift in the frequency-domain which is proportional to Ω (see properties of FT in Wikipedia). To correct for the frequency-dependent phase errors, the $S(\Omega_i)$ data points are rotated by the separate angles that vary linearly with the point index i. This stage of processing is called first-order phase correction.

Missing initial FID points during the receiver dead time may produce a spectrum baseline distortion. To correct for it, one has firstly to recognize the baseline's points among spectral peaks. Then one interpolates them and subtracts from the spectrum.

Standard NMR processing routines include peak picking and peak integration for a quantitative analysis of non-equivalent groups of spins and *J*-coupling multiplets. For the literature on the spectral analysis and available NMR software, see Further Reading.

5. Further Reading

General NMR texts:

1. A. Abragam, *"The principles of Nuclear Magnetism"*, Clarendon Press, Oxford, 1961

2. C. P. Slichter, *"Principles of Magnetic Resonance"*, Springer, Berlin, 1989

3. M. H. Levitt, *"Spin Dynamics"*, Wiley, Chichester, 2008

High-resolution NMR and spectral analysis:

4. H. Günther, *"NMR-Spectroscopie"*, Georg Thieme Verlag, Stuttgart, 1983

5. A. E. Derome, *"Modern NMR Techniques for Chemistry Research"*, Pergamon Press, Oxford, 1987

Solid-state NMR:

6. K. Schmidt-Rohr, H. W. Spiess, *"Multidimentional Solid-State NMR and Polymers"*, Academic Press, London, 1994

Spin relaxation:

7. R. Kimmich, *"NMR Tomography, Diffusometry, Relaxometry"*, Springer-Verlag, Berlin, Heidelberg, 1997

8. J. Kowalewski, L. Mäler, *"Nuclear Spin Relaxation in Liquids: Theory, Experiments and Applications"*, CRC Press, Boca Raton, Florida, 2006

On-line tutorials:

9. J. Keeler, *"Understanding NMR Spectroscopy"*, http://www-keeler.ch.cam.ac.uk/lectures/

10. J. P. Hornak, *"The basics of NMR"*, http://www.cis.rit.edu/htbooks/nmr/nmr-main.htm

11. H. J. Reich, *"Structure Determination Using Spectroscopic Methods"*,

http://www.chem.wisc.edu/areas/reich/chem605/index.htm

Other on-line resources:

12. Spectral database for organic compounds: http://sdbs.riodb.aist.go.jp/sdbs/cgi-bin/cre_index.cgi

13. Educational NMR Software: http://deane.bio.ucalgary.ca/EduNMRSoft.html

14. NMR Wiki: http://nmrwiki.org/wiki/index.php?title=Main_Page

Appendix A1. NMR Frequency Table (B$_0$ = 8.45 T)

Isotope	Symbol	Name	Spin	Natural Abund. %	Receptivity (rel. to 13C)	Magnetic Moment	Gamma (x 10^7 rad/Ts)	Quadrup. Moment Q/fm^2	Frequency	Reference
191 Ir	Iridium	3/2	37.30000	0.00001	0.19460	0.48120	81.60000	6.185	
197 Au	Gold	3/2	100.00000	0.00003	0.19127	0.47306	54.70000	6.224	
193 Ir	Iridium	3/2	62.70000	0.00002	0.21130	0.52270	75.10000	6.736	
155 Gd	Gadolinium	3/2	14.80000	---	-0.33208	-0.82132	127.00000	11.052	
103 Rh	Rhodium	1/2	100.00000	0.18600	-0.15310	-0.84680	---	11.471	Rh(acac)3 p
57 Fe	Iron	1/2	2.11900	0.00425	0.15696	0.86806	---	11.656	Fe(CO)5
157 Gd	Gadolinium	3/2	15.65000	---	-0.43540	-1.07690	135.00000	14.508	
107 Ag	Silver	1/2	51.83900	0.20500	-0.19690	-1.08892	---	14.572	AgNO3
183 W	Tungsten	1/2	14.31000	0.06310	0.20401	1.12824	---	14.999	Na2WO4
109 Ag	Silver	1/2	48.16100	0.29000	-0.22636	-1.25186	---	16.753	AgNO3
39 K	Potassium	3/2	93.25810	0.00048	0.50543	1.25006	5.85000	16.799	KCl
89 Y	Yttrium	1/2	100.00000	0.70000	-0.23801	-1.31628	---	17.641	Y(NO3)3
53 Cr	Chromium	3/2	9.50100	0.00009	-0.61263	-1.51520	-15.00000	20.349	K2CrO4
40 K	Potassium	4	0.01170	0.00000	-1.45132	-1.55429	-7.30000	20.887	KCl
201 Hg	Mercury	3/2	13.18000	0.00020	-0.72325	-1.78877	38.60000	23.802	(CH3)2HgD
14 N	Nitrogen	1	99.63200	0.00100	0.57100	1.93378	2.04400	26.015	CH3NO2
33 S	Sulfur	3/2	0.76000	0.00002	0.83117	2.05568	-6.78000	27.634	(NH4)2SO4
189 Os	Osmium	3/2	16.15000	0.00040	0.85197	2.10713	85.60000	27.955	OsO4
37 Cl	Chlorine	3/2	24.22000	0.00066	0.88320	2.18437	-6.43500	29.361	NaCl
131 Xe	Xenon	3/2	21.18000	0.00060	0.89319	2.20908	-11.40000	29.678	XeOF4
169 Tm	Thulium	1/2	100.00000	---	-0.40110	-2.21800	---	29.844	
61 Ni	Nickel	3/2	1.13990	0.00004	-0.96827	-2.39480	16.20000	32.170	Ni(CO)4
35 Cl	Chlorine	3/2	75.78000	0.00358	1.06103	2.62420	-8.16500	35.272	NaCl
135 Ba	Barium	3/2	6.59200	0.00033	1.08178	2.67550	16.00000	35.764	BaCl2
50 V	Vanadium	6	0.25000	0.00014	3.61376	2.67065	21.00000	35.893	VOCl3
15 N	Nitrogen	1/2	0.36800	0.02250	-0.49050	-2.71262	---	36.492	MeNO2
10 B	Boron	3	19.90000	0.00395	2.07921	2.87468	8.45900	38.677	BF3.Et2O
137 Ba	Barium	3/2	11.23200	0.00079	1.21013	2.99295	24.50000	40.007	BaCl2
138 La	Lanthanum	5	0.09000	0.00008	4.06809	3.55724	45.00000	47.499	LaCl3
9 Be	Beryllium	3/2	100.00000	0.01390	-1.52014	-3.75967	5.28800	50.587	BeSO4
6 Li	Lithium	1	7.59000	0.00064	1.16256	3.93717	-0.08080	52.978	LiCl
2 H	Deuterium	1	0.01150	0.00000	1.21260	4.10663	0.28600	55.262	(CD3)4Si
75 As	Arsenic	3/2	100.00000	0.02540	1.85835	4.59616	31.40000	61.641	NaAsF6
171 Yb	Ytterbium	1/2	14.28000	---	0.85506	4.72880	---	62.998	
199 Hg	Mercury	1/2	16.87000	5.89000	0.87622	4.84579	---	64.479	Me2Hgr
77 Se	Selenium	1/2	7.63000	3.15000	0.92678	5.12539	---	68.657	Me2Se
29 Si	Silicon	1/2	4.68320	2.16000	-0.96179	-5.31900	---	71.522	Me4Si
207 Pb	Lead	1/2	22.10000	11.80000	1.00906	5.58046	---	75.314	Me4Pb
111 Cd	Cadmium	1/2	12.80000	7.27000	-1.03037	-5.69831	---	76.376	Me2Cd
195 Pt	Platinum	1/2	33.83200	20.70000	1.05570	5.83850	---	77.388	Na2PtCl6
113 Cd	Cadmium	1/2	12.22000	7.94000	-1.07786	-5.96092	---	79.895	Me2Cd
69 Ga	Gallium	3/2	60.10800	0.04190	2.60340	6.43886	17.10000	86.405	Ga(NO3)3
159 Tb	Terbium	3/2	100.00000	---	2.60000	6.43100	143.20000	86.544	
79 Br	Bromine	3/2	50.69000	0.04030	2.71935	6.72562	31.30000	90.194	NaBr
13 C	Carbon	1/2	1.07000	1.00000	1.21661	6.72828	---	90.522	Me4Si
123 Te	Tellurium	1/2	0.89000	0.96100	-1.27643	-7.05910	---	94.211	Me2Te
23 Na	Sodium	3/2	100.00000	0.09270	2.86298	7.08085	10.40000	95.227	NaCl
63 Cu	Copper	3/2	69.17000	0.06500	2.87549	7.11179	-22.00000	95.456	[Cu(CH3CN)4][ClO4]
81 Br	Bromine	3/2	49.31000	0.04910	2.93128	7.24978	26.20000	97.223	NaBr
129 Xe	Xenon	1/2	26.44000	33.60000	-1.34749	-7.45210	---	100.117	XeOF4
65 Cu	Copper	3/2	30.83000	0.03540	3.07465	7.60435	-20.40000	102.253	[Cu(CH3CN)4][ClO4]
71 Ga	Gallium	3/2	39.89200	0.05710	3.30787	8.18117	10.70000	109.788	Ga(NO3)3
125 Te	Tellurium	1/2	7.07000	13.40000	-1.53894	-8.51084	---	113.579	Me2Te
11 B	Boron	3/2	80.10000	0.13200	3.47103	8.58470	4.05900	115.502	BF3.Et2O
115 Sn	Tin	1/2	0.34000	0.71100	-1.59150	-8.80130	---	117.787	Me4Sn
87 Rb	Rubidium	3/2	27.83000	0.04930	3.55258	8.78640	13.35000	117.794	RbCl
117 Sn	Tin	1/2	7.68000	20.80000	-1.73385	-9.58879	---	128.276	Me4Sn
119 Sn	Tin	1/2	8.59000	26.60000	-1.81394	-10.03170	---	134.246	Me4Sn
7 Li	Lithium	3/2	92.41000	0.27100	4.20408	10.39770	-4.01000	139.910	LiCl
31 P	Phosphorus	1/2	100.00000	391.00000	1.95999	10.83940	---	145.731	H3PO4
203 Tl	Thallium	1/2	29.52400	340.00000	2.80983	15.53933	---	205.644	Tl(NO3)3
205 Tl	Thallium	1/2	70.47600	836.00000	2.83747	15.69218	---	207.662	Tl(NO3)3
3 He	Helium	1/2	0.00014	0.00356	-3.68515	-20.38016	---	274.246	He
19 F	Fluorine	1/2	100.00000	4900.00000	4.55333	25.18148	---	338.738	CCl3F
1 H	Hydrogen	1/2	99.98850	5870.00000	4.83735	26.75221	---	360.000	Me4Si
3 H	Tritium	1/2	0.00000	---	5.15971	28.53498	---	383.990	Me4Si-t1